iScience

CellPress
OPEN ACCESS

Article

Carbon Nanotubes Enabled Laser 3D Printing of High-Performance Titanium with Highly Concentrated Reinforcement

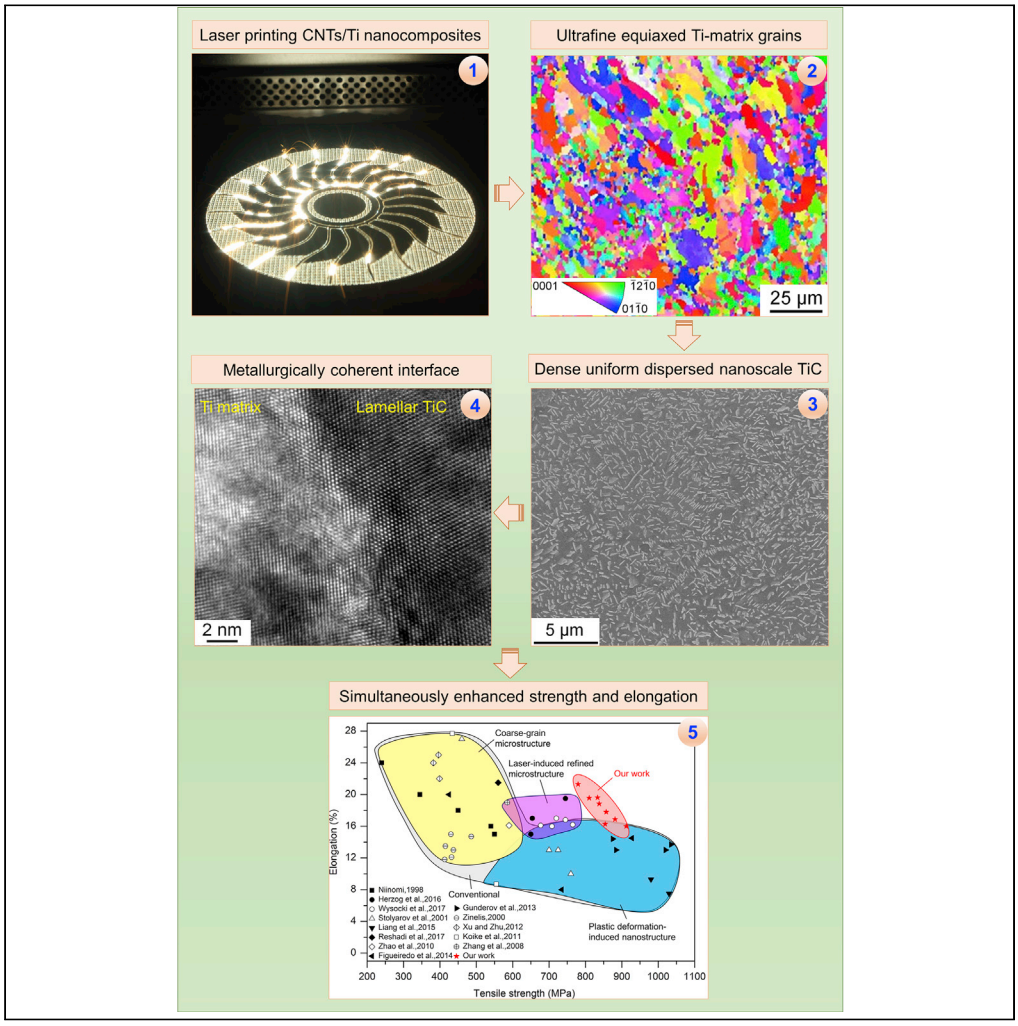

Dongdong Gu, Hongyu Chen, Donghua Dai, ..., Chen Hong, Andres Gasser, Reinhart Poprawe

dongdonggu@nuaa.edu.cn

HIGHLIGHTS

Take advantage of reaction between CNTs and Ti for performance breakthrough

Use laser 3DP as a unique route to tailor *in situ* formation of novel nanostructure

Increase strength and ductility simultaneously via multiple strengthening mechanisms

Broaden structural applications of CNTs in load-bearing Ti-based engineering materials

Gu et al., iScience *23*, 101498
September 25, 2020
https://doi.org/10.1016/j.isci.2020.101498

iScience

CellPress
OPEN ACCESS

Article

Carbon Nanotubes Enabled Laser 3D Printing of High-Performance Titanium with Highly Concentrated Reinforcement

Dongdong Gu,[1,2,5,*] Hongyu Chen,[1,2] Donghua Dai,[1,2] Chenglong Ma,[1,2] Han Zhang,[1,2] Kaijie Lin,[1,2] Lixia Xi,[1,2] Tong Zhao,[3,4] Chen Hong,[3,4] Andres Gasser,[3,4] and Reinhart Poprawe[3,4]

SUMMARY

Zero- to two-dimensional nanomaterials have been incorporated into metal-matrices to improve the strength of metals, but challengingly, high-volume-fraction nanomaterials are difficult to disperse uniformly in metal matrices, severely degrading the ductility of conventionally processed metals. Here, a considerably dense uniform dispersion of *in situ* formed nanoscale lamellar TiC reinforcement (16.1 wt %) in Ti matrix is achieved through laser-tailored 3D printing and complete reaction of Ti powder with a small amount (1.0 wt %) of carbon nanotubes (CNTs). An enhanced tensile strength of 912 MPa and an outstanding fracture elongation of 16% are simultaneously achieved for laser-printed components, showing a maximum 350% improvement in "product of strength and elongation" compared with conventional Ti. *In situ* nanoscale TiC reinforcement favors the formation of ultrafine equiaxed Ti grains and metallurgically coherent interface with minimal lattice misfit between TiC lamellae and Ti matrix. Our approach hopefully provides a feasible way to broaden structural applications of CNTs in load-bearing Ti-based engineering components via laser-tailored reorganization with Ti.

INTRODUCTION

Modern aerospace, aircraft, and automobile industries have an urgent demand for the increased payload and fuel efficiency, promoting the development of better metallic materials with higher strength/weight ratios (Pollock, 2010). Since the strength-ductility trade-off has been a long-standing dilemma for materials (Wei et al., 2014), increasing the strength of metals without sacrificing ductility is critical for their competitiveness (Lu, 2010). An essential solution of this challenge relies on a radical change in the way that metals are reinforced, which in turn calls for revolutionary production technologies. However, conventional synthesis and processing methods have reached certain limits in further elevating the properties of metals including titanium (Ti) (Chen et al., 2015). Titanium may be reinforced by other materials in a controlled way to form titanium matrix composites (TMCs), which provides a possible route to enhance overall properties (Attar et al., 2018; Dadbakhsh et al., 2019; Tian et al., 2019). Performance enhancement of novel materials also urgently calls for even advanced processing technologies. Laser-based three-dimensional printing (3DP)/additive manufacturing (AM) of metallic materials is currently attracting worldwide research interest, owing to the immense application demands in recent years from high-end industries (Bourell et al., 2017; Debroy et al., 2019; Macdonald and Wicker, 2016). Laser-based 3DP has demonstrated a significant capability for creating high-performance/multi-functional components with complex geometries in a cost-effective manner (Martin et al., 2017; Shukrun et al., 2018; Zhakeyev et al., 2017). More importantly, its highly non-equilibrium physical metallurgical nature, featured by superhigh heating/cooling rates (10^3–10^8 K s^{-1}) (Das et al., 2010), makes this technology more unique and valuable for the development of non-equilibrium nano-phases and fine-grained microstructures and attendant enhancement in final mechanical performance (Wang et al., 2018).

Ceramic nanoparticles including TiC (Gu et al., 2012b), TiB_2 (Attar et al., 2015), and B_4C (Li et al., 2019), as a category of zero-dimensional nanomaterial, have been added into Ti matrix to produce Ti-based nanocomposites by laser 3DP. Laser printing of TMCs based on external addition of ceramic reinforcing

[1]College of Materials Science and Technology, Nanjing University of Aeronautics and Astronautics, Yudao Street 29, Nanjing 210016, PR China

[2]Jiangsu Provincial Engineering Laboratory for Laser Additive Manufacturing of High-Performance Metallic Components, Nanjing University of Aeronautics and Astronautics, Yudao Street 29, Nanjing 210016, PR China

[3]Fraunhofer Institute for Laser Technology ILT, Steinbachstraße 15, Aachen 52074, Germany

[4]Chair for Laser Technology LLT, RWTH Aachen University, Steinbachstraße 15, Aachen 52074, Germany

[5]Lead Contact

*Correspondence: dongdonggu@nuaa.edu.cn

https://doi.org/10.1016/j.isci.2020.101498

particles is essentially a powder metallurgy route, with the main cores of ceramic particles remaining unmelted. Nevertheless, it is rather difficult to incorporate nanoparticles into Ti since they tend to agglomerate into clusters within the matrix, especially for a high-weight-fraction ceramic addition, thus initiating cracks in composites rather than reinforcing them (Lin et al., 2019). A large difference in surface tensions of ceramics and Ti also causes poor wettability and weak interfacial coherence of reinforcing phase by molten metal (Ma et al., 2017).

New carbonaceous nanomaterials, e.g., one-dimensional nanomaterial carbon nanotubes (CNTs) and two-dimensional nanomaterial graphene, owing to their extraordinary high specific strength (Bakshi et al., 2010), have also been introduced to strengthen Ti matrix, using both laser processes (Hu et al., 2019) and powder metallurgy routes (Li et al., 2013). Presently, the worldwide production capacity of CNTs exceeds several thousand tons per year (De Volder et al., 2013). For commercialization of CNTs products that find applications in load-bearing engineering structures, it is essential to integrate CNTs with metals to form nanocomposites (Kinloch et al., 2018). Besides the general processing difficulties of nanomaterials such as phase agglomeration and limited wettability, another long-term challenge arises from the possible chemical reaction between CNTs/graphene and Ti matrix during processing (Landry et al., 1998). A general principle of processing CNTs/graphene reinforced TMCs is to make CNTs/graphene "survive" during processing, thereby maintaining their initial nanostructural characteristics. However, owing to the extremely high atomic activity of CNTs/graphene, the *in situ* chemical reaction between C and Ti is normally inevitable during high-temperature processing. A close study of the microstructures of TMCs in previous work (Hu et al., 2019; Li et al., 2013) reveals a typical composite reinforcing structure, including the unreacted surviving CNTs/graphene and a fraction of *in situ* formed TiC during processing, hence increasing the microstructural heterogeneity.

In the present study, we propose a completely reverse processing philosophy to process CNTs/Ti TMCs, fully taking advantage of selective laser melting (SLM) 3DP to tailor an *in situ* reaction between CNTs and Ti to form novel nano-reinforcement. CNTs refer to a helical tubular structure grown with a single wall or multi-wall and typically have a diameter less than 100 nm (Bakshi et al., 2010). The high chemical activity of CNTs enables a complete *in situ* atomic-scale reaction between CNTs and Ti matrix during SLM 3DP. Thanks to the initial favorable nanostructure of CNTs, the reaction product is hopefully tailored in a nanoscale. More important, the unique physical metallurgical nature of laser 3DP, e.g., sufficiently high working temperature, superhigh temperature gradient, and superfast solidification rate, favors a homogeneous high-density precipitation of *in situ* nanophase, which is generally impossible for conventional powder metallurgy process for TMCs with limited thermodynamics. We demonstrate that a unique SLM process plus a class of new carbonaceous nanomaterial leads to a thorough reorganization of materials and attendant development of novel TMCs, yielding the significantly elevated mechanical performance of as-printed materials. We achieve a great balance between strength and ductility of TMCs via laser-tailored formation of nanoscale *in situ* reinforcement and regulation of interfacial strengthening mechanisms.

RESULTS AND DISCUSSION

Laser-Tailored Formation Mechanism of *In Situ* Nanoscale Reinforcement

Since CNTs powder demonstrates a high tendency toward agglomeration (Tjong, 2013), it is a long-standing challenge to homogenize CNTs dispersion while maintaining a high flowability of a nanocomposite powder, which plays a crucial role in achieving a smooth powder layer deposition and a sound SLM processability. We develop an approach for the scaled preparation of highly flowable and homogeneous Ti-based nanocomposite powder. Spherical CP-Ti powder is coated with CNTs powder using a "low-energy ball milling" method featured by a relatively low ball-to-powder ratio and a reduced rotational speed of grinding bowls. The original favorable spherical structure of Ti matrix powder is well maintained after ball milling (Figure 1A) to ensure a sufficiently high flowability of as-milled nanocomposite powder. CNTs are uniformly coated and distributed on the surface of Ti particles, with CNTs coating thickness being several tens of nanometers (Figures 1B–1D). Mass-produced CNTs/Ti nanocomposite powder was additively manufactured via the SLM process. We optimize an "island scanning" strategy by dividing the cross-section into islands to reduce the vector length (Figures 1E and 1F), which can greatly reduce residual stresses in SLM-processed parts. We also rotate the scan pattern by 37° in each island between neighboring layers; the directional anisotropy of current layer is compensated for by the following layers, thereby creating a more homogeneous stress and microstructure distribution (Thijs et al., 2013). SLM of our carefully prepared CNTs/Ti nanocomposite powder demonstrates a smooth laser-powder interaction

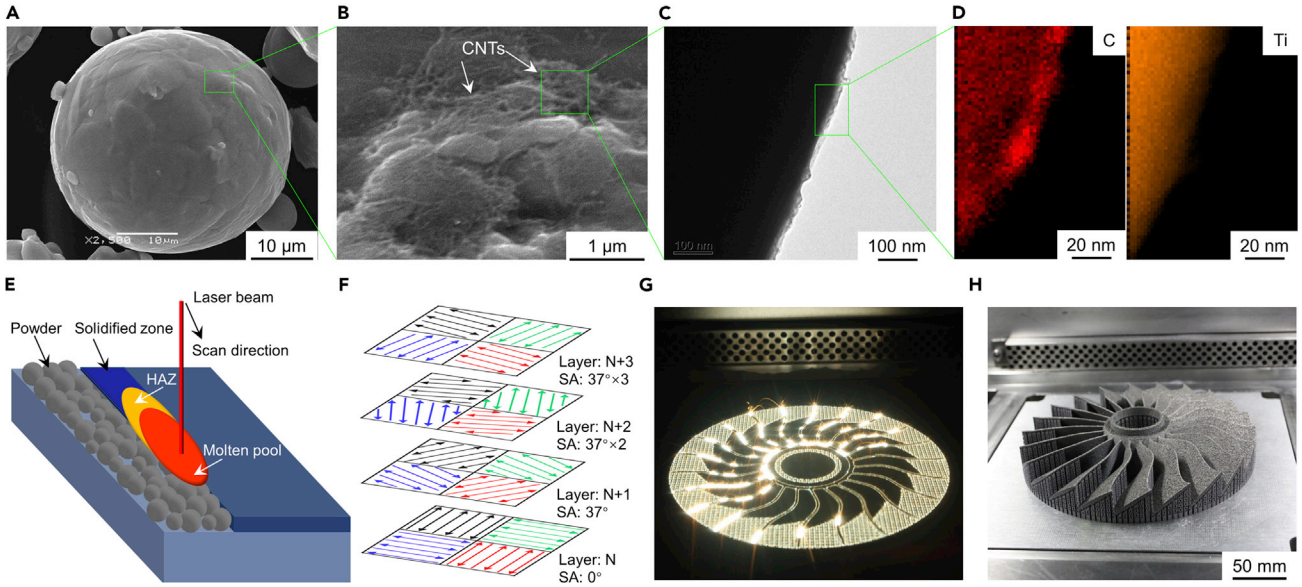

Figure 1. SLM 3D Printing of CP-Ti Powder with 1.0 wt % CNTs

(A) SEM image showing the spherical structure of Ti matrix powder after ball milling.

(B–D) (B) SEM image revealing a uniform dispersion of CNTs on Ti particle surface. Bright-field TEM image (C) with corresponding C and Ti EDS maps (D), confirming a nanoscale coating of CNTs layer on particle surface.

(E) Schematic of SLM process via layer-by-layer powder fusing and consolidation with a high-energy laser beam.

(F) "Island scanning" strategy applied for SLM.

(G) Long-exposure photo of SLM process revealing a complete laser scan profile of a layer.

(H) Laser 3D-printed Ti-based turbine with dimensions 220 mm (outer diameter) × 52 mm (height).

(Figure 1G) and a high capability to produce complex-structured integral turbine part with a dimension larger than 200 mm in a single print (Figure 1H).

Scanning electron microscope (SEM) and transmission electron microscope (TEM) characterizations of as-built Ti-based samples using a laser power of 350 W demonstrate that SLM of CNTs/Ti powder yields a completely new composite structure, showing a considerably dense uniform dispersion of the significantly refined lamellar reinforcing phase throughout Ti matrix (Figure 2B). The selected area electron diffraction (SAED) pattern of a lamella can be indexed as TiC crystal along the [001] direction on the basis of a cubic unit cell (Figure 2C), implying the occurrence of *in situ* reaction between CNTs and Ti during SLM. We accordingly propose a reverse processing philosophy on CNTs-reinforced Ti-based nanocomposites through laser-tailored reorganization of materials, fully taking advantage of conventionally "unfavorable" *in situ* reaction between CNTs and Ti matrix. Interestingly, our energy-dispersive spectroscopy (EDS) line-scan analysis across a lamella reveals a gradient distribution of C element (Figure 2D), indicating the formation of substoichiometric titanium carbide referred to as TiC_x (x = 0.1–0.9) (Hugosson et al., 2001). The substoichiometric TiC_x carbides are stable over a large range of C contents. Our TEM analysis reveals that the TiC_x lamellae generally have a standard nanostructure, with the average thickness below 80 nm (Figure 2C). We attribute the formation of nanoscale TiC_x to the combined effect of its material nature and unique thermodynamic behavior of SLM process. The standard Gibbs free energy (ΔG) of TiC formation by a reaction between titanium and carbon above the melting temperature of titanium is −136.178 kJ/mol (Barin, 1995), indicating a spontaneous generation of TiC_x during SLM. SLM is featured by a superfast melting/solidification metallurgical process, and the operative temperature within the molten pool exceeds 3,000 K within 1.1 ms, yielding an extremely high peak cooling rate of 2.73×10^7 K s^{-1} (Figure S1A). The *in situ* precipitated TiC_x nuclei have insufficient time for crystal growth, well retaining the nanostructure. Meanwhile, the calculated temperature gradient within the molten pool is as high as 4.89×10^7 K m^{-1} (Figure S1B), giving rise to surface tension gradient and resultant Marangoni flow (Leung et al., 2018). The formation of convective stream within the molten pool induces liquid capillary force, which in turn exerts on the precipitated TiC_x and accelerates its rearrangement throughout the melt, favoring a homogeneous dispersion in the solidified matrix (Figure 2B).

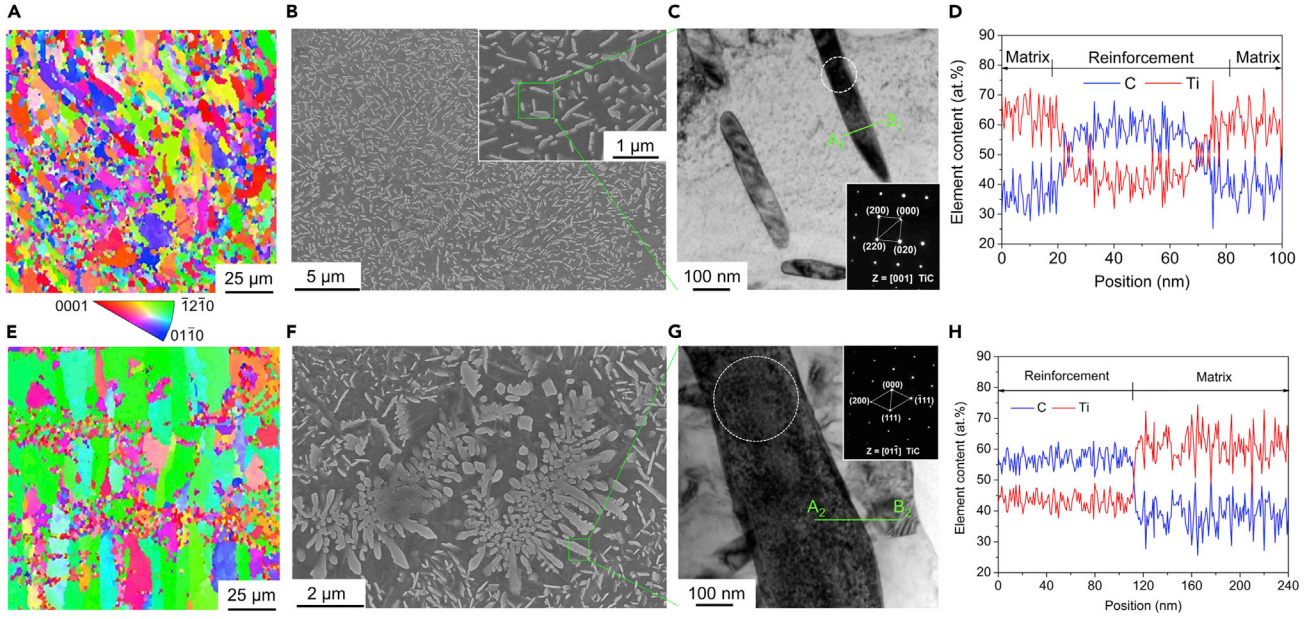

Figure 2. Microstructural Characterizations of Laser-printed Ti-based Samples Using Different Laser Powers

Laser powers of (A–D) 350 W and (E–H) 150 W are used, while laser scan speed of 1,300 mm s^{-1} is fixed.

(A and E) Cross-sectional EBSD IPF map of Ti-based samples showing grain morphologies and orientations.

(B) SEM images showing a dense uniform dispersion of the significantly refined reinforcing phase formed at a laser power of 350 W. The inset acquired at a higher magnification highlights the lamellar nanostructure of the reinforcement.

(F) SEM image showing the presence of dendritic reinforcing phase at a laser power of 150 W.

(C and G) Bright-field TEM images and SAED patterns (on white dotted circles) of the lamellar reinforcement formed at 350 W and the dendritic arm formed at 150 W.

(D and H) EDS line scan across reinforcement and matrix (along green lines A_1B_1 and A_2B_2) showing concentration distributions of C and Ti elements.

We further study the grain morphology and size distribution of Ti matrix by electron backscatter diffraction (EBSD). The inverse-pole figure (IPF) map shows an almost general formation of fine equiaxed Ti grains at a laser power of 350 W (Figure 2A), yielding a relatively large fraction of low-angle grain boundaries (LAGBs, 2°–15°) of ~17% (Figure S2A). The estimated average grain size of Ti matrix, 3.24 μm, is considerably low (Figure S2B). A successive change of color in the IPF map reveals that the crystallographic orientation of Ti grains is highly random (Figure 2A). Here we demonstrate that the *in situ* formation of nanoscale TiC_x reinforcement exerts a significant effect on microstructural development of Ti matrix during a non-equilibrium SLM process, featured by the prevailing of refined grain size, enhanced fraction of LAGBs, and week texture intensity.

Effect of Printing Parameters on Microstructural and Interfacial Characteristics

We conduct intensive experiments on process optimization and find that the microstructural development of reinforcement is very sensitive to the applied printing parameters. Although SLM at a relatively low laser power of 150 W also leads to the *in situ* formation of TiC reinforcing phase, as confirmed by SAED pattern (Figure 2G), its microstructure experiences a substantial change into a dendritic structure with a dendrite trunk length larger than 6 μm (Figure 2F), completely losing the novel nanoscale lamellar structure formed at a laser power of 350 W (Figure 2B). The C and Ti elemental distribution from the dendritic arm of reinforcement to the matrix becomes flattened, which changes abruptly in the reinforcement/matrix interface (Figure 2H). The dendritic TiC is accordingly supposed to be stoichiometric and maturely developed, showing little compositional gradient. We observe a major presence of the apparently coarsened columnar Ti grains with a preferred crystallographic orientation of <$\bar{1}2\bar{1}0$> along the building direction (green region, Figure 2E). As relative to the printed specimen at 350 W, the maximum texture intensity increased nearly twice (Figures S2C and S3C), indicating a much stronger <$\bar{1}2\bar{1}0$> texture in this instance. The columnar grains are separated by the high-angle grain boundaries (HAGBs) (Figure S3A), exhibiting a wider grain size distribution and an elevated average size of 3.97 μm (Figure S3B). We infer that the solute fields of

carbon during non-equilibrium laser solidification determine the morphologies of TiC. SLM at a laser power of 150 W produces a relatively low thermal gradient of 2.01 × 10^7 K m^{-1} (Figure S1B) and attendant weak activity of solute atoms, building up a solute boundary layer at the solid-liquid interface owing to a high carbon solute concentration. The constitutional supercooling thus occurs, causing a morphological instability of the solid-liquid interface (Kim, 1978). The amplitude of the perturbation increases with the TiC_x crystal growth proceeds. The finally developed TiC phase accordingly demonstrates a dendritic growth mechanism.

Of particular interest is that laser power has an essential influence on growth morphologies of TiC reinforcing phase. A reasonable increase in laser power favors the morphological transformation of TiC from a coarsened dendritic structure to a refined nanoscale lamellar structure (Figure 2B versus 2F); nevertheless, the TiC becomes re-coarsened into a rod-like shape at an excessive laser power of 450 W (Figure S4C), caused by an elevated thermalization of laser energy and attendant enhanced growth kinetics of TiC_x nuclei. We also disclose that, as a sufficiently high laser power of 350 W is optimized, the lamellar structured TiC reinforcement is generally produced at various laser scan speeds. Nevertheless, we still discern a minor morphological difference. A proper increase in laser scan speed refines the TiC lamellae and homogenizes its distribution in the matrix (Figure S4D versus S4B); however, an excessively high scan speed of 1,700 mm s^{-1} produces the re-coarsened and agglomerated TiC lamellae (Figure S4F). The elevated Marangoni convection and liquid capillary instability in the molten pool formed at a higher laser scan speed intensify the microstructural heterogeneity of as-printed Ti-based nanocomposites.

We demonstrate that the development manner of *in situ* TiC significantly affects its atomic bonding ability with Ti matrix. The atomic map of the interface between dendritic TiC and Ti matrix, consisting of (0002) planes of Ti and (200) planes of TiC, illustrates an evidently sharp interface (Figures 3A and 3B) and attendant disordered and unfavorable dendrite/matrix atomic bonding (Figure 3C). We measure the spacing between the adjacent lattice planes and the lattice misfit of two phases was calculated to be 9.2% in this instance. By contrast, the interface between lamellar TiC and Ti matrix is considerably coherent (Figures 3D and 3E), indicating a continuous and metallurgically compatible atomic bonding (Figure 3F). By measuring the interplanar spacing of $(10\bar{1}1)$ planes of Ti matrix and (200) planes of TiC lamella, we find that the lattice misfit between the nanoscale lamellar TiC and Ti matrix decreases significantly to 1.9%.

Nanoscale Reinforcement Induced Microstructural Development of Ti Matrix

We further performed X-ray diffraction (XRD) to investigate the constitutional phases and examine the grain refinement and lattice mismatch in SLM-processed Ti-based nanocomposites. The strong diffraction peaks corresponding to TiC and hexagonal close-packed (hcp) Ti are generally identified in the specimens printed at different laser powers. Here we determine that starting from 1.0 wt % CNTs, the content of *in situ* TiC_x in 350-W-printed Ti-based specimen increases dramatically to ~16.1 wt %. A close look at the diffraction peak for TiC (111) (350 W, 1,300 mm s^{-1}), which locates at 2θ of 36.451°, reveals that the lattice parameter of TiC is a = 0.427 nm. This observation confirms that the *in situ* formed nanoscale substoichiometric titanium carbide is $TiC_{0.3}$ (Harada and Ohkoshi, 1997). Because of the considerably short laser melting time, the carbon atoms do not have sufficient time to diffuse into the TiC_x lattice to form stoichiometric TiC (Al-Mangour et al., 2017). A large number of interstitial carbon sites therefore remain vacant. This can explain why the incorporation of a low-weight fraction of CNTs to Ti can achieve a highly concentrated precipitation of TiC_x nanoscale reinforcing phase within matrix. The XRD characterization within a small 2θ range (inset in Figure 4A) illustrates that, as relative to the standard diffraction peaks for hcp-Ti (α-phase) located at 2θ of 35.17°, the exact 2θ locations of the diffraction peaks for hcp-Ti in laser-printed nanocomposites generally shift to lower 2θ angles, indicating an increase in interplanar distance based on the Bragg's law (Gu et al., 2012a). Normally, the occurrence of martensitic transformation is accompanied by microscopic volume expansion, thereby enhancing the distortion of lattice and resultant lattice constant. Our quantitative calculation reveals the lattice parameters a = 0.29529 nm and c = 0.46912 nm for 350-W-printed specimen, which are apparently larger than the standard lattice parameters a_0 = 0.2944 nm and c_0 = 0.4678 nm of α-Ti (Rostoker, 1952). These hcp-Ti diffraction peaks accordingly correspond to martensitic α'-phase, induced by the direct transformation of β-Ti to α'-Ti during laser rapid melting/solidification process (Collins et al., 2016). It is worth noting that a more significant shift of α'-Ti peak to a lower 2θ angle occurs in laser-printed Ti-based nanocomposites using a higher laser power of 350 W, which implies a lager degree of lattice distortion caused by the incorporation of densely dispersed nanoscale lamellar TiC_x in the Ti matrix.

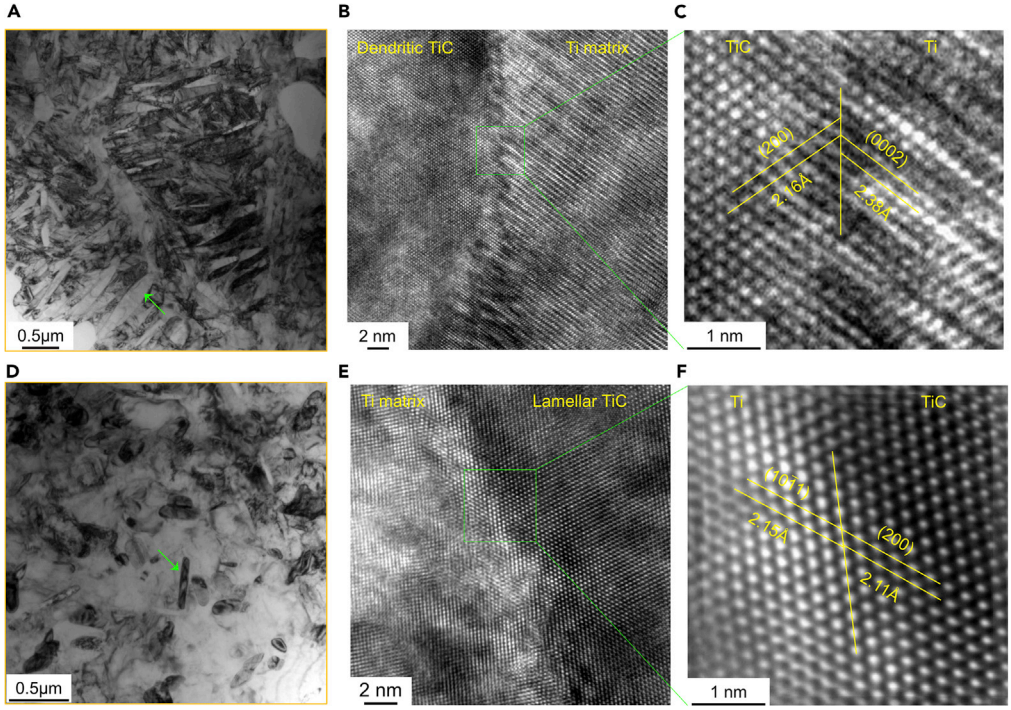

Figure 3. Growth Mechanisms and Resultant Interfacial Microstructures of *In Situ* TiC Reinforcing Phase in SLM-Processed Ti-Based Nanocomposites Using Different Laser Powers

(A and D) TEM images showing the formation of dendritic TiC at laser power of 150 W (A) and lamellar TiC at laser power of 350 W (D). The arrows in (A) and (D) indicate the positions for the analysis of reinforcement/matrix interfaces.

(B and C) HR-TEM images revealing a limited interfacial continuity (B) and atomic coherence between dendritic TiC and Ti matrix (C) at a laser power of 150 W.

(E and F) HR-TEM images showing coherent interface (E) and atomic structure between lamellar TiC and Ti matrix (F) at a laser power of 350 W.

Lattice strain is a measure of the distribution of lattice constants arising from crystal imperfections such as lattice distortion and dislocations (Yogamalar et al., 2009). To quantitatively analyze the lattice strain, we display the modified Williamson-Hall plots of $\sin\theta$ versus $\beta_{hkl}\cdot\cos\theta$ in Figure 4B, where $\beta_{hkl}\cdot\cos\theta$ is the width of XRD diffraction peaks and θ is the Bragg angle. From the linear fit to the data, we extract the lattice strain and grain size of α'-Ti from the slope and Y-intercept of the fit line, respectively, where the lattice strain is assumed to be uniform in all crystallographic orientations. We disclose that the application of a higher laser power gives rise to a larger lattice strain of the Ti matrix, as the slope of the red fit line (0.52107 for 350-W printed specimen) is larger than that of the blue fit line (0.18895 for 150-W printed specimen). Meanwhile, a smaller value of Y intercept of red line implies that the grain refinement effect is more significant in the specimen printed at 350 W, which is consistent with the EBSD data (Figure S2A versus S3A). A high-density distribution of *in situ* formed TiC_x lamellae ahead of the solidification front in the molten pool provides numerous low-energy-barrier heterogeneous nucleation sites for the Ti matrix, favoring the equiaxed growth of crystals and attendant ultrafine microstructure. We observe the significantly refined, lath-shaped martensitic microstructure of α'-Ti matrix (Figure 4C) and the high-density dislocations within the martensitic laths (Figures 4D and 4E). Owing to the incorporation of densely distributed nanoscale *in situ* TiC reinforcement, the α'-Ti matrix accordingly demonstrates a combined effect of large lattice distortion, significant grain refinement, and high-density dislocations.

Tensile Properties and Strengthening Mechanisms

We perform tensile tests and compare the results with specimens produced from CP-Ti by conventional processing methods (Figure 5A). The laser-printed *in situ* Ti-based nanocomposites with a small amount (0.5–1.0 wt %) CNTs addition have high tensile strengths, which are almost two times stronger than those of conventional coarsen-grained CP-Ti parts. Of particular significance is that the laser-printed *in situ* Ti-based nanocomposites maintain sufficiently high ductility, demonstrating a significantly elevated balance

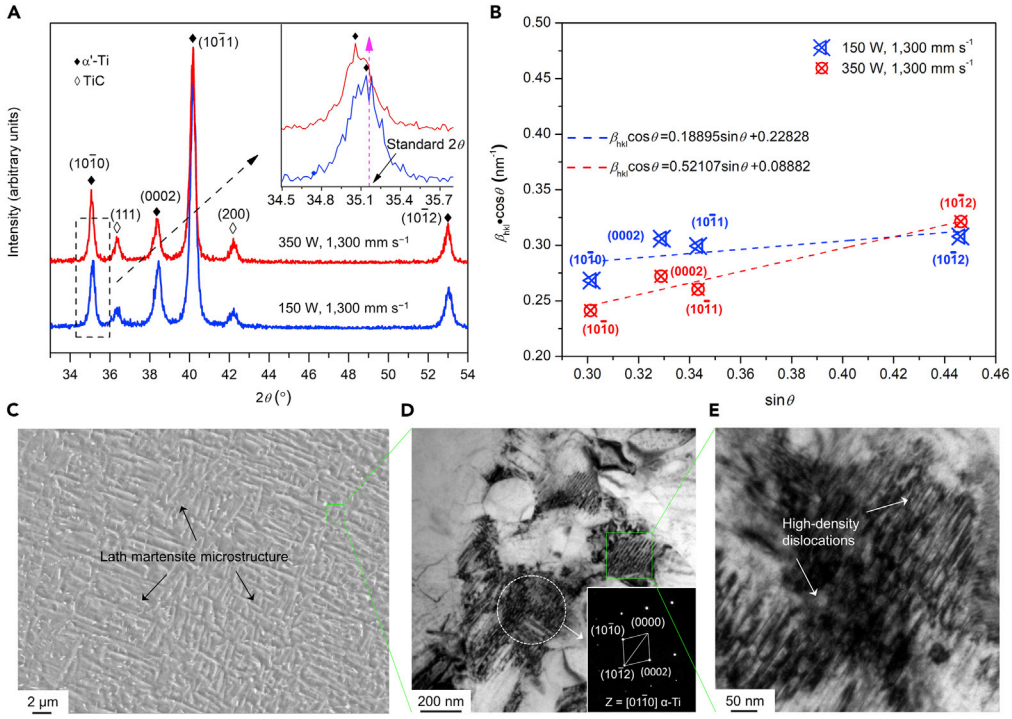

Figure 4. Phase and Microstructure Analysis of Titanium Matrix in SLM-Processed Nanocomposites

(A) XRD patterns of specimens using different printing parameters.

(B) Modified Williamson-Hall plots for specimens. The dash-dotted lines are the linear fits obtained by a method of least squares, depicting the different lattice distortions induced by dislocations and grain refinement effect under different laser processing conditions.

(C and D) SEM (C) and TEM (D) images of the characteristic ultrafine lath martensite structure of α′-Ti matrix in specimen printed at 350 W.

(E) Magnified TEM image showing the presence of high-density dislocations within martensite laths of Ti matrix.

between strength and ductility. Therefore, tailoring the *in situ* formation of nanoscale TiC reinforcement throughout the Ti matrix dramatically improves the overall mechanical properties without sacrificing the ductility of the nanocomposites. We provide in Figure 5B five representative tensile engineering stress-strain curves of laser-processed Ti-based nanocomposites and CP-Ti extracted from Figure 5A. With an addition of 0.5 wt % CNTs, a simultaneous improvement in tensile strength of 799 MPa and fracture elongation of 21% is achieved for laser-printed specimen at 350 W, compared with the laser-printed CP-Ti prepared at the same processing parameter (tensile strength of 735 MPa and elongation 19.6%). The Young's moduli deduced from tensile stress-strain curves of laser-printed Ti-based nanocomposites with 0.5 wt % CNTs vary from 96 to 107 GPa. With the additive CNTs increased to 1.0 wt %, laser-printed nanocomposites yield a better strength of 912 MPa by a slight sacrificing of elongation to 16%. Since more nanoscale TiC_x reinforcement form within laser-printed Ti-based nanocomposites, the Young's modulus increases to a higher value within 104–118 GPa. As relative to coarse dendritic TiC with an intrinsic brittle nature formed at a low laser power (Figure 3A), the homogeneously dispersed, ultrafine nanoscale TiC reinforcement obtained via a high-laser-power printing can effectively transfer load owing to their favorable interfacial atomic bonding with α′-Ti matrix (Figure 3D–3F). Here we apply a key performance indicator "product of strength and elongation" (PSE) to indicate the balance between strength and ductility. The PSE of the optimally printed Ti-based nanocomposites reaches 16.8 GPa·%, showing a maximum 350% improvement in PSE as relative to conventionally processed unreinforced CP-Ti.

To understand the deformation behaviors and strengthening mechanisms of laser-printed *in situ* Ti-based nanocomposites, we perform microstructural characterizations on tensile samples at different strain levels. Dislocation slipping plays a dominant role in the deformation at a relatively low tensile strain of 3%. The nanoscale lamellar TiC reinforcing phase tends to hinder the movement of dislocations and activates the Orowan effect,

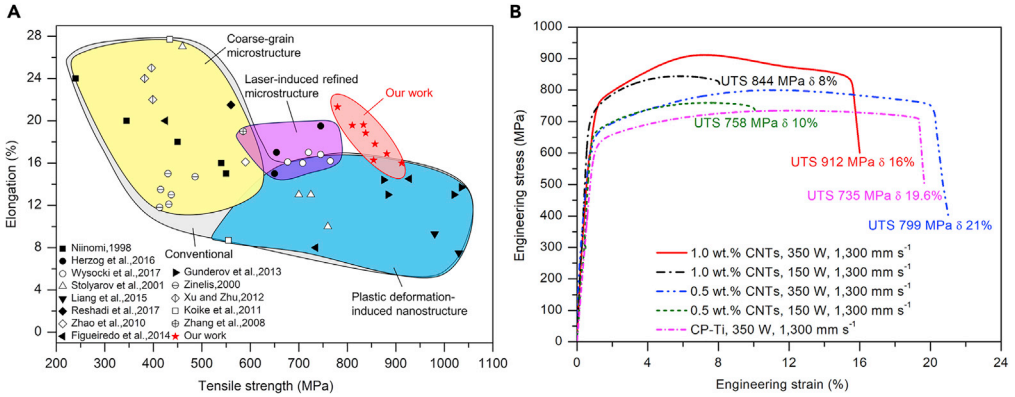

Figure 5. Tensile Properties of Laser 3D-Printed *In Situ* Ti-Based Nanocomposite Parts

(A) A summary of tensile strength versus fracture elongation of Ti processed by various methods, including our work (red region), laser additive manufactured Ti with refined microstructure (purple region) (Herzog et al., 2016; Wysocki et al., 2017; Zhang et al., 2008), conventional coarse-grained Ti processed by casting and forging (yellow region) (Koike et al., 2011; Stolyarov et al., 2001; Xu and Zhu, 2012; Niinomi, 1998; Reshadi et al., 2017; Figueiredo et al., 2014; Zhao et al., 2010; Zinelis, 2000), Ti strengthened through plastic deformation with the formation of nanostructure (blue region) (Gunderov et al., 2013; Liang et al., 2015). The error bar of each experimental datum from our work is depicted in Figure S5.

(B) Typical engineering stress-strain curves for tensile tests. The ultimate tensile strength (UTS, σ_b) and fracture elongation (δ) are indicated on the curves.

resulting in the trapping and pileup of dislocations around TiC lamellae with a further deformation (Figure 6A). It is known that the strengthening mechanism through grain refinement predominates for SLM-processed CP-Ti without any reinforcement and the grain refinement normally leads to reduction of twining propensity (Attar et al., 2014). Differently, a small amount of deformation twins, which are generally present near the zones with a considerably high dislocation density, are also observed in the present Ti-based nanocomposites in this strain level (Figures 6B and 6C). As the strain level increases to 8%, twinning becomes a predominant mechanism responsible for the further deformation. More importantly, these twins show a nano-sized structural feature (nano-twins). The nano-twins restrict the transmission of dislocations from one side of the twin boundary (TB) to the other (Zhu et al., 2007). Therefore, compared with the low strain level, the pileup of dislocations becomes more significant near the TiC lamellae, further producing the stress concentration zones under the action of a tensile load (Figure 6E). Numerous sets of nano-twins nucleate and develop around the lamellar TiC (Figures 6D and 6F) when the stress concentration reaches the twin critical value (Zhu et al., 2007). Once the deformation dominated by dislocation slipping is hard to proceed, the subsequently present nano-twins lead to the formation of twinning-induced lattice reorientation, where TBs can act as slip planes on which dislocations move and pile up. The dislocation slip along TBs releases effectively the stress concentration at the dislocation-TB intersection region, thereby accumulating a large amount of plastic strain for a high density of TBs (Lu et al., 2009). This slip-within-twin mechanism favors an additional plastic deformation, significantly improving the deformability and achievable ductility of Ti-based nanocomposites.

Conclusions

The SLM 3DP process, owing to its unique material additive manufacturing philosophy and highly non-equilibrium physical and chemical metallurgical nature, provides a one-step approach to create complex structured, new nanocomposite components with unique reinforcement architectures and elevated mechanical properties. With the aid of SLM 3DP, an addition of a small amount of CNTs (1.0 wt %) to CP-Ti enables a dramatic *in situ* formation of Ti-based nanocomposites having a dense uniform dispersion of 16.1 wt % nanoscale lamellar TiC reinforcement. An enhanced tensile strength of up to 912 MPa and a high fracture elongation of 16% are simultaneously achieved for laser-printed *in situ* Ti-based nanocomposites, showing a maximum 350% improvement in PSE as relative to conventional CP-Ti. Strengthening of Ti-based nanocomposites is based on coherent interface and minimal lattice misfit between nanoscale TiC lamellae and Ti matrix through a synergistic function of multiple strengthening mechanisms including dislocation slipping and deformation twinning. A great balance between strength and ductility is achieved via laser-tailored formation of nanoscale reinforcement and interfacial regulation. Our approach hopefully broadens the structural applications of CNTs, whose worldwide production capacity has exceeded several

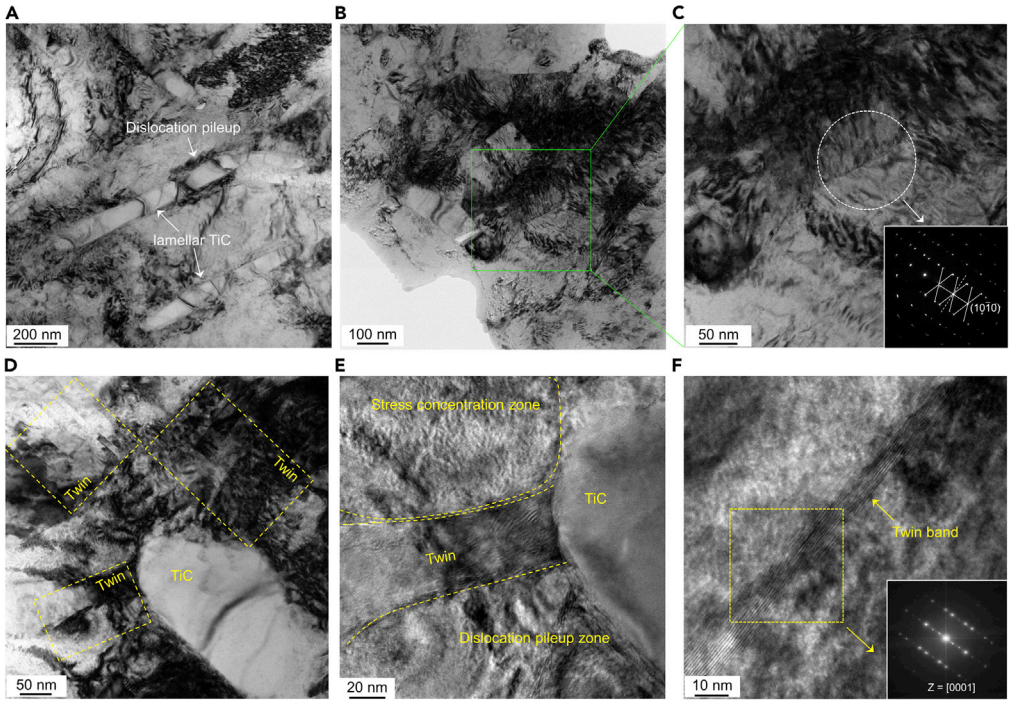

Figure 6. Microstructural Characterization of Laser 3D-Printed Ti-Based Nanocomposite Part at Different Tensile Strains during Tensile Test

(A–C) Representative deformation microstructures at 3% tensile strain. (A) Bright-field TEM image showing the dislocation pileup effect induced by lamellar TiC during the early stage of deformation. (B and C) Bright-field TEM images showing the origination of deformation twins nucleated from the zones with high-density dislocations. The inset in (C) shows a symmetrical SAED pattern of the corresponding deformation twin, revealing a {10-10} type of twin.

(D–F) Representative deformation microstructures at 8% tensile strain. (D) Bright-field TEM image showing the significant formation of deformation twins around lamellar TiC. (E) Magnified bright-field TEM image of the interface between lamellar TiC and twins, revealing the roles of stress concentration zone and dislocation pileup zone in the formation of deformation twins. (F) HR-TEM image showing the formation of twin band. The inset is the fast Fourier transform (FFT) pattern taken from the yellow dotted square in (F), revealing a symmetric diffraction pattern oriented to the [0001] zone axis and attendant formation of deformation twins.

thousand tons per year, in load-bearing Ti-based engineering components via laser-tailored reorganization with Ti materials that are served as cornerstone of modern aircraft, aerospace, and energy industries.

Limitations of the Study

For reaction-based 3DP method for formation of TiC-reinforced Ti-based nanocomposites, the influence of the initial carbon source on laser-tailored formation of TiC reinforcement needs to be further considered. Besides the CNTs being studied in this work, the nanoscale carbon sources can be broadened to graphite nanoparticles and even graphene. The effects of the type, structure, and size of the carbon matter on the laser printability and resultant microstructural and mechanical properties of laser-printed Ti-based nanocomposites deserve to be further studied. Second, besides the matrix metal titanium studied in this work, other metals having carbide-forming ability can also be mixed with carbon sources for laser printing to yield the carbide-reinforced metal matrix nanocomposites. Third, as a unique heat source, laser plays an important role in tailoring *in situ* reaction and forming metal matrix nanocomposites. In addition to the fiber laser being applied in this study, more new lasers can be applied for more potential breakthroughs in microstructure control and performance enhancement.

Resource Availability

Lead Contact

Further information and requests for materials should be directed to and will be fulfilled by the lead contact, Dongdong Gu (dongdonggu@nuaa.edu.cn).

Materials Availability

All new unique reagents generated in this study are available from the lead contact with a completed materials transfer agreement.

Data and Code Availability

The published article includes all datasets generated or analyzed during this study.

METHODS

All methods can be found in the accompanying Transparent Methods supplemental file.

SUPPLEMENTAL INFORMATION

Supplemental Information can be found online at https://doi.org/10.1016/j.isci.2020.101498.

ACKNOWLEDGMENTS

The work was supported by the National Natural Science Foundation of China (grant no. 51735005); the Key Project of Equipment Pre-research Fund (grant no. 61409230311); the National Key Research and Development Program of China "Additive Manufacturing and Laser Manufacturing" (grant numbers 2016YFB1100101 and 2018YFB1106302); and the NSFC-DFG Sino-German Research Project (grant no. GZ 1217). D.G. acknowledges the support from the National High-level Personnel of Special Support Program of China; the Cheung Kong Young Scholars Program of Ministry of Education of China; the Top-Notch Young Talents Program of China; and the Fraunhofer-Bessel Research Award from Alexander von Humboldt Foundation Germany.

AUTHOR CONTRIBUTIONS

D.G. conceived the idea and designed the study. D.G., H.C., D.D., and L.X. prepared nanocomposite powder. D.G., H.C., D.D., H.Z., T.Z., and C.H. conducted laser additive manufacturing experiments. H.C., D.D., and C.M. developed theoretical models and methods for simulation. H.C., D.G., C.M., and K.L. characterized microstructures and properties. D.G., H.C., A.G., and R.P. analyzed the data. D.G. wrote the paper. D.G. and R.P. supervised the whole work.

DECLARATION OF INTERESTS

The authors declare no competing interests.

Received: June 3, 2020
Revised: July 30, 2020
Accepted: August 20, 2020
Published: September 25, 2020

REFERENCES

AlMangour, B., Grzesiak, D., and Yang, J.M. (2017). In-situ formation of novel TiC-particle-reinforced 316L stainless steel bulk-form composites by selective laser melting. J. Alloys Compd. *706*, 409–418.

Attar, H., Calin, M., Zhang, L., Scudino, S., and Eckert, J. (2014). Manufacture by selective laser melting and mechanical behavior of commercially pure titanium. Mater. Sci. Eng. A *593*, 170–177.

Attar, H., Ehtemam-Haghighi, S., Kent, D., and Dargusch, M.S. (2018). Recent developments and opportunities in additive manufacturing of titanium-based matrix composites: a review. Int. J. Mach. Tools Manuf. *133*, 85–102.

Attar, H., Prashanth, K.G., Zhang, L., Calin, M., Okulov, I.V., Scudino, S., Yang, C., and Eckert, J. (2015). Effect of powder particle shape on the properties of in situ Ti-TiB composite materials produced by selective laser melting. J. Mater. Sci. Technol. *31*, 1001–1005.

Bakshi, S.R., Lahiri, D., and Agarwal, A. (2010). Carbon nanotube reinforced metal matrix composites - a review. Int. Mater. Rev. *55*, 41–64.

Barin, I. (1995). Thermochemical Data of Pure Substances, Third Edition (VCH Verlagsgesellschaft mbH), p. 1674.

Bourell, D., Kruth, J.P., Leu, M., Levy, G., Rosen, D., Beese, A.M., and Clare, A. (2017). Materials for additive manufacturing. CIRP Ann. Manuf. Technol. *66*, 659–681.

Chen, L.Y., Xu, J.Q., Choi, H., Pozuelo, M., Ma, X., Bhowmick, S., Yang, J.M., Mathaudhu, S., and Li, X.C. (2015). Processing and properties of magnesium containing a dense uniform dispersion of nanoparticles. Nature *528*, 539–543.

Collins, P.C., Brice, D.A., Samimi, P., Ghamarian, I., and Fraser, H.L. (2016). Microstructural control of additively manufactured metallic materials. Annu. Rev. Mater. Res. *46*, 63–91.

Dadbakhsh, S., Mertens, R., Hao, L., Humbeeck, J., and Kruth, J.-P. (2019). Selective laser melting to manufacture "in situ" metal matrix composites: a review. Adv. Eng. Mater. *21*, 1801244.

Das, M., Balla, V.K., Basu, D., Bose, S., and Bandyopadhyay, A. (2010). Laser processing of SiC-particle-reinforced coating on titanium. Scripta Mater. *63*, 438–441.

De Volder, M.F.L., Tawfick, S.H., Baughman, R.H., and Hart, A.J. (2013). Carbon nanotubes: present

and future commercial applications. Science *339*, 535–539.

Debroy, T., Mukherjee, T., Milewski, J.O., Elmer, J.W., Ribic, B., Blecher, J.J., and Zhang, W. (2019). Scientific, technological and economic issues in metal printing and their solutions. Nat. Mater. *18*, 1026–1032.

Figueiredo, R.B., Barbosa, E.R.D., Zhao, X.C., Yang, X.R., Liu, X.Y., Cetlin, P.R., and Langdon, T.G. (2014). Improving the fatigue behavior of dental implants through processing commercial purity titanium by equal-channel angular pressing. Mater. Sci. Eng. A *619*, 312–318.

Gu, D., Hagedorn, Y.C., Meiners, W., Meng, G., Batista, R., Wissenbach, K., and Poprawe, R. (2012a). Densification behavior, microstructure evolution, and wear performance of selective laser melting processed commercially pure titanium. Acta Mater. *60*, 3849–3860.

Gu, D., Meng, G., Li, C., Meiners, W., and Poprawe, R. (2012b). Selective laser melting of TiC/Ti bulk nanocomposites: influence of nanoscale reinforcement. Scripta Mater. *67*, 185–188.

Gunderov, D.V., Polyakov, A.V., Semenova, I.P., Raab, G.I., Churakova, A.A., Gimaltdinova, E.I., Sabirov, I., Segurado, J., Sitdikov, V.D., Alexandrov, I.V., et al. (2013). Evolution of microstructure, macrotexture and mechanical properties of commercially pure Ti during ECAP-conform processing and drawing. Mater. Sci. Eng. A *562*, 128–136.

Harada, T., and Ohkoshi, H. (1997). Growth and structure of Ti films deposited on chemically polished MgO(100) substrates. J. Cryst. Growth *171*, 433–441.

Herzog, D., Seyda, V., Wycisk, E., and Emmelmann, C. (2016). Additive manufacturing of metals. Acta Mater. *117*, 371–392.

Hu, Z., Wang, D., Chen, C., Wang, X., Chen, X., and Nian, Q. (2019). Bulk titanium–graphene nanocomposites fabricated by selective laser melting. J. Mater. Res. *34*, 1744–1753.

Hugosson, H.W., Korzhavyi, P., Jansson, U., Johansson, B., and Eriksson, O. (2001). Phase stabilities and structural relaxations in substoichiometric TiC_{1-x}. Phys. Rev. B *63*, 165116.

Kim, K.M. (1978). Morphological instability under constitutional supercooling during the crystal growth of InSb from the melt under stabilizing thermal gradient. J. Cryst. Growth *44*, 403–413.

Kinloch, I.A., Suhr, J., Lou, J., Young, R.J., and Ajayan, P.M. (2018). Composites with carbon nanotubes and graphene: an outlook. Science *362*, 547–553.

Koike, M., Martinez, K., Guo, L., Chahine, G., Kovacevic, R., and Okabe, T. (2011). Evaluation of titanium alloy fabricated using electron beam melting system for dental applications. J. Mater. Process. Technol. *211*, 1400–1408.

Landry, K., Kalogeropoulou, S., and Eustathopoulos, N. (1998). Wettability of carbon by aluminum and aluminum alloys. Mater. Sci. Eng. A *254*, 99–111.

Leung, C.L.A., Marussi, S., Atwood, R.C., Towrie, M., Withers, P.J., and Lee, P.D. (2018). In situ X-ray imaging of defect and molten pool dynamics in laser additive manufacturing. Nat. Commun. *9*, 1355.

Li, H., Yang, Z., Cai, D., Jia, D., and Zhou, Y. (2019). Microstructure evolution and mechanical properties of selective laser melted bulk-form titanium matrix nanocomposites with minor B4C additions. Mater. Des. *185*, 108245.

Li, S., Sun, B., Imai, H., Mimoto, T., and Kondoh, K. (2013). Powder metallurgy titanium metal matrix composites reinforced with carbon nanotubes and graphite. Compos. Part A Appl. Sci. Manuf. *48*, 57–66.

Liang, C., Ma, M., Jia, M., Raynova, S., Yan, J., and Zhang, D. (2015). The tensile mechanical properties of thermomechanically consolidated titanium at different strain rates. Metall. Mater. Trans. A Phys. Metall. Mater. Sci. *46A*, 5095–5102.

Lin, T.C., Cao, C., Sokoluk, M., Jiang, L., Wang, X., Schoenung, J., Lavernia, E., and Li, X. (2019). Aluminum with dispersed nanoparticles by laser additive manufacturing. Nat. Commun. *10*, 4124.

Lu, K. (2010). The future of metals. Science *328*, 319–320.

Lu, K., Lu, L., and Suresh, S. (2009). Strengthening materials by engineering coherent internal boundaries at the nanoscale. Science *324*, 349–352.

Ma, C., Chen, L., Cao, C., and Li, X. (2017). Nanoparticle-induced unusual melting and solidification behaviours of metals. Nat. Commun. *8*, 14178.

Macdonald, E., and Wicker, R. (2016). Multiprocess 3D printing for increasing component functionality. Science *353*, aaf2093.

Martin, J.H., Yahata, B.D., Hundley, J.M., Mayer, J.A., Schaedler, T.A., and Pollock, T.M. (2017). 3D printing of high-strength aluminium alloys. Nature *549*, 365–369.

Niinomi, M. (1998). Mechanical properties of biomedical titanium alloys. Mater. Sci. Eng. A *243*, 231–236.

Pollock, T.M. (2010). Weight loss with magnesium alloys. Science *328*, 986–987.

Reshadi, F., Faraji, G., Baniassadi, M., and Tajeddini, M. (2017). Surface modification of severe plastically deformed ultrafine grained pure titanium by plasma electrolytic oxidation. Surf. Coat. Technol. *316*, 113–121.

Rostoker, W. (1952). Observations on the lattice parameters of the alpha and TiO phases in the titanium–oxygen system. JOM *4*, 981–982.

Shukrun, E., Cooperstein, I., and Magdassi, S. (2018). 3D–printed organic–ceramic complex hybrid structures with high silica content. Adv. Sci. *5*, 1800061.

Stolyarov, V., Zhu, Y., Alexandrov, I.V., Lowe, T., and Valiev, R. (2001). Influence of ECAP routes on microstructure and properties of pure Ti. Mater. Sci. Eng. A Struct. *299*, 59–67.

Thijs, L., Kempen, K., Kruth, J.-P., and Humbeeck, J. (2013). Fine-structured aluminium products with controllable texture by selective laser melting of pre-alloyed AlSi10Mg powder. Acta Mater. *61*, 1809–1819.

Tian, W., VahidMohammadi, A., Reid, M., Wang, Z., Ouyang, L., Erlandsson, J., Pettersson, T., Wågberg, L., Beidaghi, M., and Hamedi, M. (2019). Multifunctional nanocomposites with high strength and capacitance using 2D MXene and 1D nanocellulose. Adv. Mater. *31*, 1902977.

Tjong, S. (2013). Recent progress in the development and properties of novel metal matrix nanocomposites reinforced with carbon nanotubes and graphene nanosheets. Mater. Sci. Eng. R Rep. *74*, 281–350.

Wang, Y., Voisin, T., McKeown, J., Ye, J., Calta, N., Li, Z., Zeng, Z., Zhang, Y., Chen, W., Roehling, T., et al. (2018). Additively manufactured hierarchical stainless steels with high strength and ductility. Nat. Mater. *17*, 63–71.

Wei, Y., Li, Y., Zhu, L., Liu, Y., Lei, X., Wang, G., Wu, Y., Mi, Z., Liu, J., Wang, H., and Gao, H. (2014). Evading the strength–ductility trade-off dilemma in steel through gradient hierarchical nanotwins. Nat. Commun. *5*, 3580.

Wysocki, B., Maj, P., Krawczyńska, A., Zdunek, J., Rożniatowski, K., Kurzydłowski, K.J., and Święszkowski, W. (2017). Microstructure and mechanical properties investigation of CP titanium processed by selective laser melting (SLM). J. Mater. Process. Technol. *241*, 13–23.

Xu, C., and Zhu, W. (2012). Comparison of microstructures and mechanical properties between forging and rolling processes for commercially pure titanium. Trans. Nonferrous Met. Soc. China *22*, 1939–1946.

Yogamalar, R., Ramasamy, S., Vinu, A., Ariga, K., and Bose, A. (2009). X-ray peak broadening analysis in ZnO nanoparticles. Solid State Commun. *149*, 1919–1923.

Zhakeyev, A., Wang, P., Zhang, L., Shu, W., Wang, H., and Xuan, J. (2017). Additive manufacturing: unlocking the evolution of energy materials. Adv. Sci. *4*, 1700187.

Zhang, Y., Wei, Z., Shi, L., and Xi, M. (2008). Characterization of laser powder deposited Ti–TiC composites and functional gradient materials. J. Mater. Process. Technol. *206*, 438–444.

Zhao, X., Yang, X., Liu, X., Wang, X., and Langdon, T. (2010). The processing of pure titanium through multiple passes of ECAP at room temperature. Mater. Sci. Eng. A Struct. *527*, 6335–6339.

Zhu, T., Li, J., Samanta, A., Kim, H.G., and Suresh, S. (2007). Interface plasticity governs strain rate sensitivity and ductility in nanostructured metals. Proc. Natl. Acad. Sci. U S A *104*, 3031–3036.

Zinelis, S. (2000). Effect of pressure of helium, argon, krypton, and xenon on the porosity, microstructure, and mechanical properties of commercially pure titanium castings. J. Prosthet. Dent. *84*, 575–582.

iScience, Volume *23*

Supplemental Information

Carbon Nanotubes Enabled Laser 3D Printing of High-Performance Titanium with Highly Concentrated Reinforcement

Dongdong Gu, Hongyu Chen, Donghua Dai, Chenglong Ma, Han Zhang, Kaijie Lin, Lixia Xi, Tong Zhao, Chen Hong, Andres Gasser, and Reinhart Poprawe

SUPPLEMENTAL INFORMATION

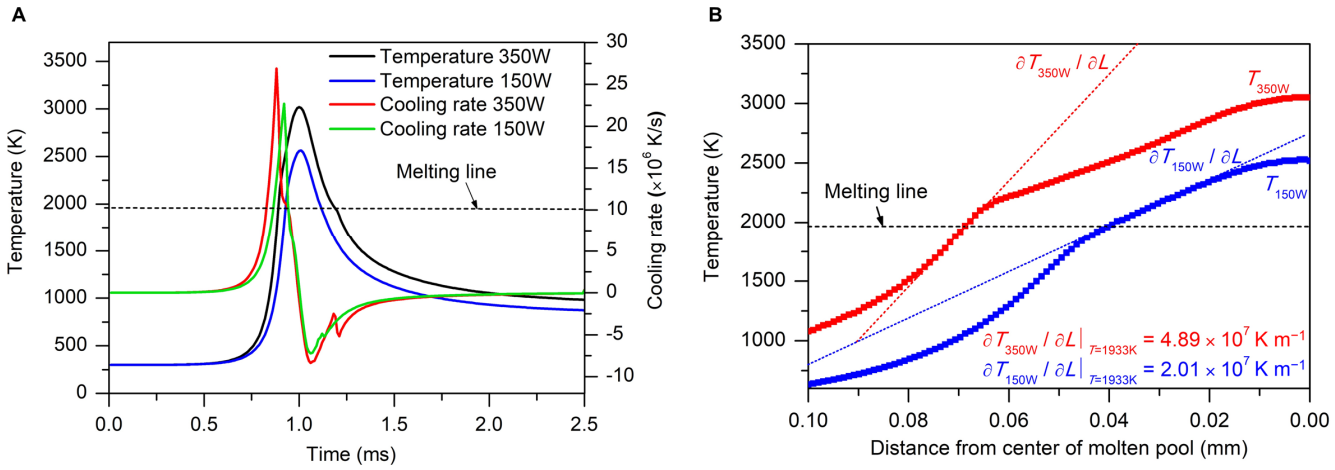

Figure S1. Finite volume method (FVM) simulation of thermal evolution behavior of molten pool during SLM of 1.0 wt.% CNTs/Ti nanocomposite powder using different laser powers. (**A**) Profiles of temperature evolution and attendant cooling rate of molten pool during solidification. (**B**) Profiles of temperature versus distance from the center of molten pool and the corresponding temperature gradient at solid/liquid interface within molten pool. Parameters for simulation of SLM of Ti-based nanocomposite powder in the FVM model included: laser spot size of 70 μm, laser powers of 150 W and 350 W, laser scan speed of 1,300 mm s^{-1}, hatch spacing of 40 μm, powder layer thickness of 40 μm and ambient temperature of 300 kelvin (K). Related to Figure 2.

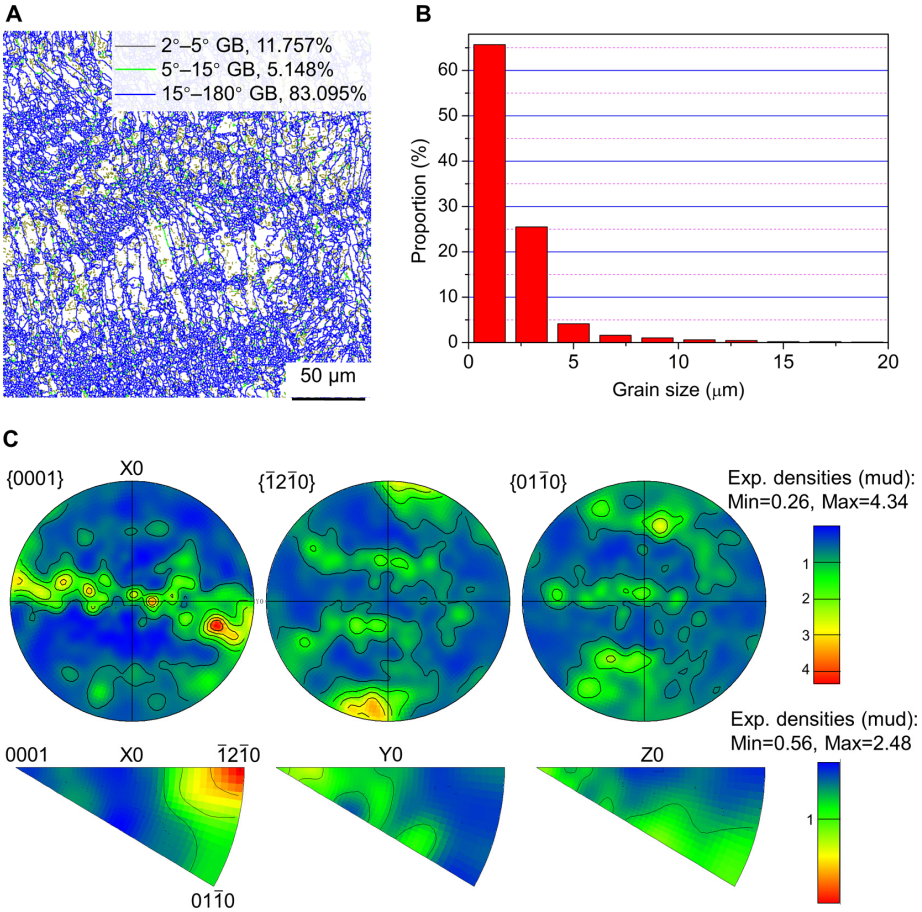

Figure S2. Crystallographic analysis of grains and grain boundaries (GBs) in SLM-processed Ti-based sample using a laser power of 350 W and a scan speed of 1,300 mm s^{-1}. (**A**) Cross-sectional EBSD GB map on the ultrafine equiaxed grains with high-angle grain boundaries (HAGBs) (blue), low-angle grain boundaries (LAGBs) (green) and subgrain boundaries (grey) superimposed. The building direction of the sample in this image is vertical. (**B**) Distribution of grain sizes of as-built Ti-based sample revealed by EBSD measurement. (**C**) Pole figures (above) and inverse pole figures (below) for as-printed Ti-based sample. Related to Figure 2.

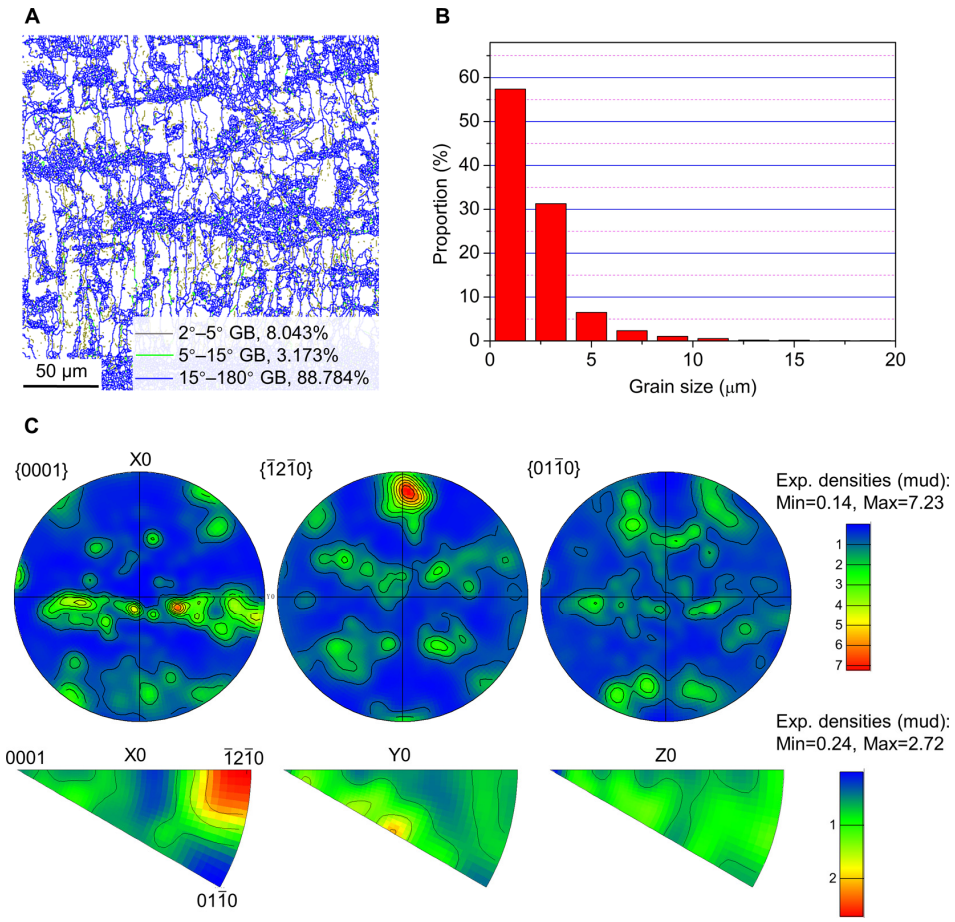

Figure S3. Crystallographic analysis of grains and grain boundaries (GBs) in SLM-processed Ti-based sample using a relatively low laser power of 150 W and a scan speed of 1,300 mm s^{-1}. (**A**) Cross-sectional EBSD GB map on the typical columnar grains with HAGBs (blue), LAGBs (green) and subgrain boundaries (grey) superimposed. The building direction of the sample in this image is vertical. (**B**) Distribution of grain sizes of as-built Ti-based sample revealed by EBSD measurement. (**C**) Pole figures (above) and inverse pole figures (below) for the printed Ti-based sample. Related to Figure 2.

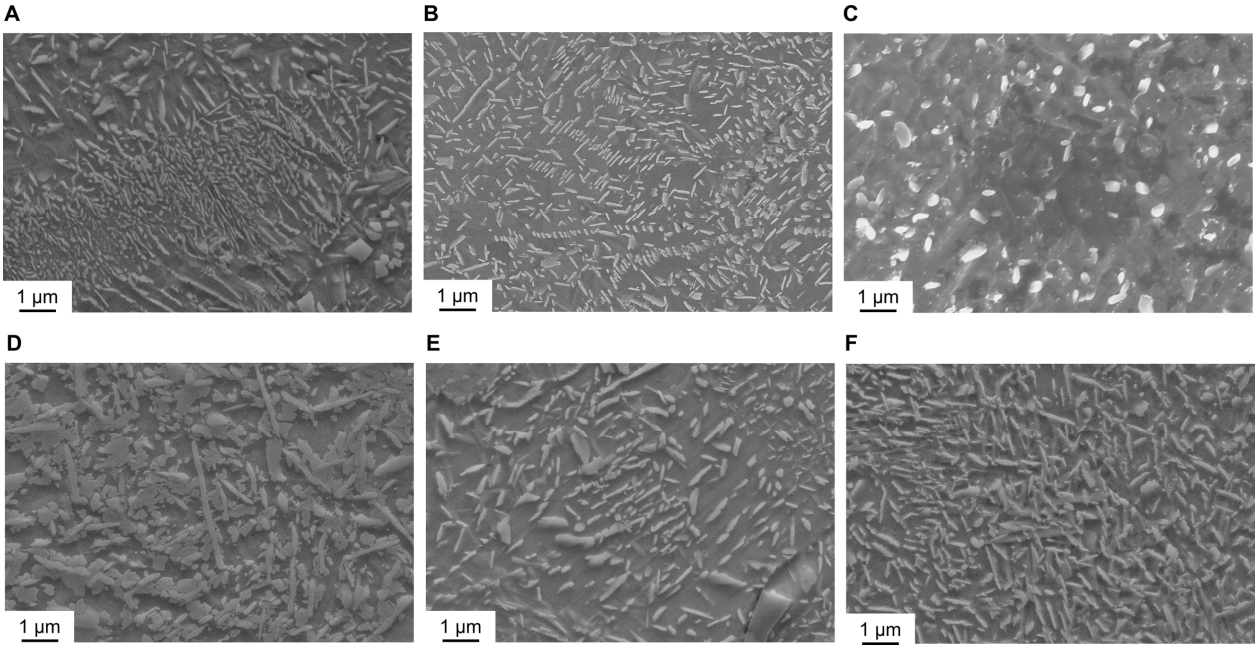

Figure S4. Effects of laser power and scan speed on microstructural development of in-situ TiC reinforcement in SLM-processed Ti-based samples. (**A**) The refined dendritic structure at 250 W; (**B**) the considerably refined nanoscale lamellar structure at 350 W; (**C**) the re-coarsened rod-like structure at 450 W. An optimal laser scan speed was kept constant at 1,300 mm s^{-1} for this batch of specimens in order to highlight the exclusive influence of laser power. (**D**) The agglomerated and coarsened TiC lamellae at 500 mm s^{-1}; (**E**) the gradually refined and dispersed TiC lamellae at 900 mm s^{-1}; (**F**) the slightly agglomerated and coarsened TiC lamellae at 1,700 mm s^{-1}. A sufficiently high laser power of 350 W was optimized for this batch of experiments in order to realize a general formation of lamellar structured TiC reinforcing phase. Related to Figure 2 and Figure 3.

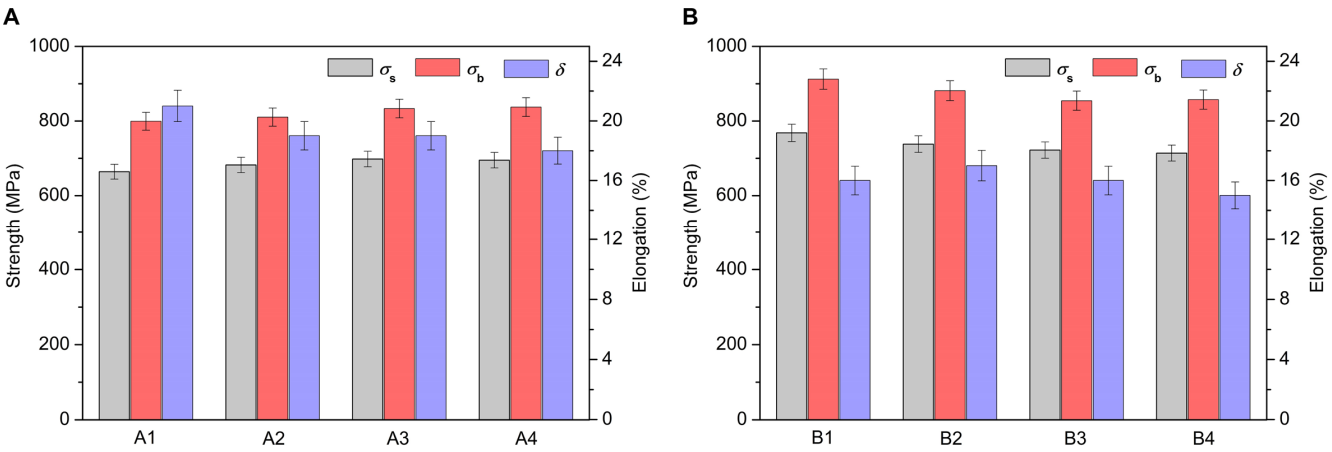

Figure S5. Effects of CNTs contents and laser printing parameters on yield strength (σ_s), ultimate tensile strength (UTS, σ_b) and fracture elongation (δ) of the tensile samples reported in Figure 5A. (**A**) Ti-based samples with 0.5 wt.% CNTs addition. Laser printing parameters are: A1 sample, laser power P=350 W, scan speed v=1,300 mm s^{-1}, hatch spacing h=50 μm; A2 sample, P=350 W, v=1,500 mm s^{-1}, h=50 μm; A3 sample, P=375 W, v=1,700 mm s^{-1}, h=50 μm; A4 sample, P=400 W, v=1,800 mm s^{-1}, h=50 μm. (**B**) Ti-based samples with 1.0 wt.% CNTs addition. Laser printing parameters are: B1 sample, P=350 W, v=1,300 mm s^{-1}, h=40 μm; B2 sample, P=375 W, v=1,400 mm s^{-1}, h=40 μm; B3 sample, P=375 W, v=1,600 mm s^{-1}, h=40 μm; B4 sample, P=425 W, v=1,800 mm s^{-1}, h=40 μm. Related to Figure 5.

TRANSPARENT METHODS

Materials

Commercially pure (CP) titanium (Ti) powder. CP-Ti powder (American Society for Testing and Materials, ASTM, Grade 1) was supplied by TLS Technik GmbH, Germany. The powder consisted of Ti (balance), N (0.005%), C (0.01%), H (0.002%), Fe (0.16%) and O (0.09%), in weight percent (wt.%). The CP-Ti powder had a spherical shape and a particle size distribution of 15–53 μm, with a mean particle size of 39.6 μm.

Carbon nanotubes (CNTs) powder. Multi-walled CNTs powders with a purity larger than 95% were supplied by abcr GmbH, Germany and Chengdu Organic Chemicals Co. Ltd., Chinese Academy of Sciences, China. The CNTs powders had an outside diameter of 8–15 nm, a length of 10–50 μm and a specific surface area (SSA) larger than 180 m^2/g.

CNTs/Ti nanocomposite powder. Two batches of CNTs/Ti nanocomposite powder consisting of 0.5 wt.% and 1.0 wt.% CNTs were prepared respectively in a Pulverisette 4 vario-planetary ball mill (Fritsch GmbH, Germany), using a ball-to-powder weight ratio of 2:1 and a rotation speed of main disk of 200 rpm. The operative milling time was set at 4 h and a ball-milling duration of 20 min was followed by an interval time of 10 min, in order to avoid the temperature rise within the grinding bowls. To avoid oxidation of the powder, the milling treatment was under the protection of an argon atmosphere within the bowls.

Selective Laser Melting (SLM)

Laser additive manufacturing of as-prepared CNTs/Ti nanocomposite powder was performed on two SLM machines developed by Nanjing University of Aeronautics and Astronautics (NUAA) and Fraunhofer Institute for Laser Technology (ILT), respectively. These two machines had the basically same configurations, consisting mainly of a single mode, continuous wave modulated YLR-500-SM ytterbium fiber laser with a maximum

power of 500 W and a spot size of 70 μm (IPG Laser GmbH, Germany), a hurrySCAN 30 scanner (SCANLAB GmbH, Germany) with a scan speed up to 7.0 m/s, an automatic flexible powder spreading mechanism with carbon fibers braided brush, an inert argon gas protection system, and software tools to manage and control 3D printing process. As specimens were to be built, a titanium substrate was fixed on the building platform and fitted precisely with the powder spreading brush. The building chamber was then sealed and the argon gas was fed inside, decreasing the O_2 content below 10 ppm. Afterward, the CNTs/Ti nanocomposite powder was deposited on the substrate by the layering mechanism, with the powder layer thickness of 40 μm. The laser beam was controlled by the software data to scan the powder bed surface selectively, producing a two-dimensional consolidated profile. An 'island scanning' strategy was applied by dividing the cross-section of a specimen into islands with a 5 mm × 5 mm size to reduce the vector length. The scan angle (SA) was rotated with 37º in each island between neighboring layers (Figure 1F). Samples of 10 mm × 10 mm × 8 mm blocks were built using a wide range of SLM parameters, i.e., laser powers of 100–400 W and scan speeds of 400–2,000 mm s^{-1}, for SLM parameters optimization by examining densification and microstructures. Specimens of 70 mm (length) × 12 mm (width) × 6 mm (height) tensile blocks were further prepared using the optimized parameters that enabled to achieve a SLM densification larger than 99.5%. The 70 mm × 12 mm rectangular plates of specimens were built parallel to the underlying substrate. The completed specimens were removed from the machine and cleaned of residual powder by compressed dry air.

X-Ray Diffraction (XRD)

Phase identification was conducted by XRD using a D8 Advance X-ray diffractometer (Bruker AXS GmbH, Germany) with Cu K_α radiation at 40 kV and 40 mA, using a continuous scan mode at 1°/min. A slower scan rate of 0.01°/min was further applied over 2θ=34°–36° to obtain a more accurate determination of diffraction peaks. XRD was

utilized to evaluate peak broadening with grain size and lattice strain due to dislocations, using the modified form of Williamson-Hall plot as follows (Yogamalar et al., 2009):

$$\beta_{\mathrm{hkl}} \cos\theta = \left(\frac{k\lambda}{D_{\mathrm{v}}}\right) + (4\varepsilon \sin\theta) \tag{1}$$

where D_{v} is the volume weighted crystallite size, k is the shape factor (0.9), λ is the wavelength of Cu K_{α} radiation, β_{hkl} is the instrumental corrected integral breadth of the reflection (in radians) located at 2θ, and θ is the angle of reflection (in degrees). Equation (1) represents a uniform deformation model (UDM), where the strain was assumed to be uniform in all crystallographic directions (Yogamalar et al., 2009). From the linear fit to the data, as shown in Figure 4b, the crystallite size was extracted from the Y-intercept and the lattice strain was deduced from the slope of the fit. The weight fraction of *in-situ* formed TiC, W_{TiC}, within the TiC/Ti dual-phase system was calculated by XRD analysis as follows (Chung, 1974):

$$W_{\mathrm{TiC}} = \frac{I_{\mathrm{TiC}}/K_{\mathrm{TiC}}}{I_{\mathrm{TiC}}/K_{\mathrm{TiC}} + I_{\mathrm{Ti}}/K_{\mathrm{Ti}}} \tag{2}$$

where I_{TiC} and I_{Ti} are the diffraction intensities of TiC and Ti phases, and K_{TiC} and K_{Ti} are constants related to the materials and can be found in JCPDS Card No. 71-0298 and JCPDS Card No. 89-2959.

Microstructural Characterization

Laser-printed parts were removed from the building plates using wire electro discharge machining (EDM). Samples for metallographic examinations was ground with 320, 600, 1,000, 1,200 and 2,000 grit sand paper. Final polishing of the samples was performed using 0.5 μm diamond polishing agent. The polished samples were etched with a solution consisting of HF (5 ml), HNO_3 (15 ml) and H_2O (150 ml) for 20 s to reveal microstructures. Microstructures were characterized using a S-4800 field emission scanning electron microscope (FE-SEM; Hitachi, Ltd., Japan). Electron backscatter diffraction (EBSD) was performed in a Nova™ NanoSEM 430 FE-SEM (FEI Company,

USA). A typical scan area of 2 mm × 2 mm on the cross-sections of laser-printed specimens was used for EBSD analysis with a scanning step size of 0.5 μm. EBSD data were analyzed using the Orientation Imaging Microscopy (OIM) analysis software provided by EDAX. Interfaces between grains were divided into three categories: sub-grain boundaries when the misorientation angle was 2°–5°, low-angle grain boundaries (LAGBs) when the misorientation angle was 5°–15°, and high-angle grain boundaries (HAGBs) with the misorientation angle of 15°–180°. To calculate the grain size, each grain was approximated as a sphere to reveal the grain diameter. Transmission electron microscope (TEM) specimens were prepared by standard electropolishing techniques. Bright-field (BF), dark-field (DF) and high-resolution (HR) TEM and corresponding selected area electron diffraction (SAED) analyses were conducted in a FEI Tecnai G2 F20 TEM operated at 200 kV with a point-to-point resolution less than 0.2 nm. The lattice misfit δ between Ti matrix and TiC reinforcing phase was calculated by:

$$\delta = (d_{\mathrm{Ti}} - d_{\mathrm{TiC}})/d_{\mathrm{Ti}} \quad (3)$$

where d_{Ti} and d_{TiC} are interplanar spacings of Ti and TiC phases at the interface. The chemical concentration maps were acquired by energy-dispersive spectroscopy (EDS) in TEM, using a Bruker QUANTAX Silicon Drift Detector (SDD) operated at an accelerating voltage of 200 kV.

Mechanical Testing

Uniaxial tensile tests were performed at room temperature in a CMT5205 tensile machine (MTS Industrial Systems, China) equipped with a 100 kN load cell. The dog-bone-shaped tensile samples (gauge length: 25.0±0.1 mm, width: 6.0±0.1 mm, thickness: 5.0 mm) were prepared according to ASTM E8 standard. The extension velocity of the cross head was 0.2 mm/min and the specimens were loaded continuously until fracture. The loading direction of the tensile samples is perpendicular to the SLM building direction. Six tensile specimens were tested for each selected laser printing parameter to yield standard error

bars. In order to disclose the deformation behaviors of laser-printed parts subjected to uniaxial loading, the deformation microstructures at different levels of ~3% and ~8% tensile strains were characterized by a FEI Tecnai G2 F20 TEM operated at 200 kV. A series of BF-TEM, HR-TEM and SAED images were recorded to reveal the deformation behavior and underlying strengthening mechanisms of specimens from multiple scales.

Numerical Simulation

The thermodynamic behavior during SLM of CNTs/Ti nanocomposite powder was simulated to reveal the formation conditions for *in-situ* Ti-based composites during laser rapid solidification. A continuous three-dimensional geometry of Ti-based nanocomposites was established and adaptively meshed by the definition of wall conditions using a Gambit software. The defined geometry was imported into a FLUENT software using a finite volume method (FVM) model. The laser energy with a Gaussian distribution was defined as a heat flux applied onto the free surface of powder bed considering the laser penetration depth. Three categories of coupled heat transfer mechanisms including the heat irradiation to powder layer from laser beam, the heat conduction among powder particles, and the heat convection between molten pool and ambient atmosphere were considered in the model. The energy, mass and momentum transformation were loaded on the top surface and the multiphase interface of the physical model. More details about the FVM model, calculation process and data extraction can be found in our previous work (Dai and Gu, 2015; Gu and Yuan, 2015; Yu et al., 2016).

SUPPLEMENTAL REFERENCES

Chung, F.H. (1974). Quantitative interpretation of X-ray diffraction pattern of mixtures. I and II. J. Appl. Cryst. *7*, 519–531.

Dai, D., and Gu, D. (2015). Tailoring surface quality through mass and momentum transfer Modeling using a volume of fluid method in selective laser melting of TiC/AlSi10Mg powder. Int. J. Mach. Tools Manuf. *88*, 95–107.

Gu, D., and Yuan, P. (2015). Thermal evolution behavior and fluid dynamics during laser additive manufacturing of Al-based nanocomposites: Underlying role of reinforcement weight fraction. J. Appl. Phys. *118*, 233109.

Yogamalar, R., Ramasamy, S., Vinu, A., Ariga, K., and Bose, A. (2009). X-ray peak broadening analysis in ZnO nanoparticles. Solid State Commun. *149*, 1919–1923.

Yu, G., Gu, D., Dai, D., Xia, M., Ma, C., and Shi, Q. (2016). On the role of processing parameters in thermal behavior, surface morphology and accuracy during laser 3D printing of aluminum alloy. J. Phys. D. Appl. Phys. *49*, 135501.